Multi-stage scheme for non-linear Breit-Wheeler pair-production utilising ultra-intense laser-solid interactions

M J Duff[1], R Capdessus[1], C P Ridgers[2] and P McKenna[1]

[1]SUPA, Department of Physics, University of Strathclyde, Glasgow, G4 0NG, UK
[2]York Plasma Institute, Department of Physics, University of York, YO10 5DD, UK

E-mail: matthew.duff@strath.ac.uk, remi.capdessus@strath.ac.uk, christopher.ridgers@york.ac.uk, paul.mckenna@strath.ac.uk

January 2019

Abstract.

Multi-petawatt (PW) lasers enable intensities exceeding 10^{23} Wcm^{-2}, at which point quantum electrodynamics (QED) processes, such as electron-positron pair-production via the non-linear Breit-Wheeler process, will play a significant role in laser-plasma interactions. Using 2D QED-particle-in-cell simulations, we present a two-stage scheme in which non-linear pair-production is induced via an ultra-intense laser-solid interaction. The first stage is the generation of a γ-ray beam, through the interaction of an ultra-intense laser pulse with a thick target, whose features are found to be strongly dependent on collective plasma effects. This compact, high energy γ-ray beam (characterised by a divergence half-angle $\sim 10^\circ$ and average photon energy $\sim$ 10 MeV) then interacts with two counter-propagating laser pulses. By varying the laser polarisation and angle of incidence, we show that in the case of two circularly polarised laser pulses propagating at an angle equal to the divergence half-angle of the γ-ray beam, the produced positron distribution is highly anisotropic compared to the case of a standard head-on collision.

Keywords: Pair-production; non-linear Breit-Wheeler process; ultra-intense laser-solid interactions
Submitted to: *Plasma Phys. Control. Fusion*

1. Introduction

The investigation of the interplay between plasma physics and quantum electrodynamics (QED) is an active research area, made possible in recent years by increases in peak laser intensities and the acceleration of particles to ultra-relativistic energies. Multi-petawatt (PW) laser facilities, such as APOLLON [1] and ELI [2], are expected to deliver peak

laser intensities exceeding 10^{23} Wcm^{-2}. At these ultra-high intensities, there are two key QED processes which influence the laser-plasma interactions: high energy radiation generation, inherently accompanied by its non-linear back reaction, and the production of electron-positron pairs. In the framework of classical electrodynamics, the radiation reaction (RR) is the recoil force exerted on an accelerated electron in a strong field, due to the (synchrotron-like) radiation it emits [3, 4, 5, 6, 7]. These photons can have sufficiently high energy to decay into electron-positron pairs within the laser field. In the presence of ultra-intense laser fields, the pair-production mainly occurs via the non-linear (or multi-photon) Breit-Wheeler process [8, 9, 10].

QED plasma physics effects become significant when the magnitude of the laser electric field, experienced in the rest frame of a relativistic particle within the plasma, is comparable to the Sauter-Schwinger critical field, given by $E_{crit} = m_e^2 c^3/e\hbar = 1.6 \times 10^{18}$ Vm^{-1} [11, 12] where m_e, e are the electron mass and charge, c is the speed of light and $\hbar$ is the reduced Planck constant. The magnitude of the electric fields produced at the highest intensities achievable at multi-PW laser facilities will be of the order 10^{15} Vm^{-1}, still well below the critical limit. Using head-on collisions with relativistic particles however, the field strength in the rest frame of the particle is boosted by the Doppler effect, therefore enhancing the amplitude of the QED effects. Typically, laser-induced pair-production studies use the process of laser wakefield acceleration (LWFA) to generate GeV electrons [13, 14, 15].

Recent experimental studies have evidenced RR [16, 17, 18], notably in the collision of a GeV electron beam with an intense, counter-propagating laser pulse [17, 18]. At upcoming multi-PW laser facilities, it will be possible to probe RR effects further by exploring the onset of quantum effects. Similarly, pair plasmas have been generated under laboratory conditions, through the interaction of ultra-intense laser pulses with high Z targets [19, 20]. A widely reported example of laser-induced pair-production is the SLAC E144 experiment, in which a 46.6 GeV electron beam collided with a relativistic laser pulse, producing a small number of positrons (~ 100) via the non-linear Breit-Wheeler process [21, 22].

In this article we present an alternative scheme for investigating laser-induced pair-production, which can be used to verify the results obtained from LWFA experiments and extend these investigations into the highly non-linear regime. This scheme involves a two-step process, in which a γ-ray beam (with high average photon energy and low divergence) is generated via an ultra-intense laser-solid interaction, and then interacts in a counter-propagating geometry with various configurations of secondary laser pulses. Here, the term counter-propagating refers to the fact that the laser pulses propagate in the opposite direction to the γ-ray beam, however the lasers are off-set from the central axis by a characteristic angle, chosen to be equal to the divergence half-angle of the γ-ray beam. We find that this interaction geometry not only enhances the number of positrons produced compared to a head-on interaction, but that the resulting positron distribution is also highly anisotropic. Such a positron source could have potential applications in laboratory astrophysics experiments.

The results presented in this article fit into a growing scheme of research in which high frequency probe beams (such as laser pulses) are employed to induce pair-production [23, 24, 25]. Additional studies have also investigated pair-production via the interaction of ultra-intense laser pulses with radiation sources, which are themselves produced via laser-solid interactions [26, 27, 28]. The novelty of our scheme lies in the fact that we induce multi-photon pair-production, via the non-linear Breit-Wheeler process, as opposed to the single photon pair-production schemes investigated in the aforementioned studies.

The structure of the article is as follows. We begin by describing the implementation of important QED processes in the Particle-In-Cell (PIC) code, EPOCH [29], in section 2. The simulation results are then presented in section 3 in two stages. First we investigate the properties of the γ-ray beam produced during the laser-solid interaction. We then investigate different configurations in which this beam interacts with counter-propagating laser pulses, with the aim of generating electron-positron pairs via the non-linear Breit-Wheeler process. Finally, we compare the configurations introduced in this article to more conventional setups, which are likely to be among the first experiments conducted at multi-PW laser facilities.

2. Numerical approach

2.1. Numerical model

The simulations are run using the fully-relativistic QED-PIC code, EPOCH [29]. The generation of synchrotron-like radiation and electron-positron pairs are handled by a Monte-Carlo algorithm [30]. At the start of the simulation, the particles in the plasma (electrons, positrons and photons) are randomly assigned a final optical depth for which an emission process (photon emission or electron-positron pair-production) will occur. The process of RR is treated using a semi-classical approach, where the radiating electron follows a classical trajectory in between photon emission events. If an emission event occurs, the photon momentum is subtracted from the momentum of the electron [31]. The electron (and positron) trajectory is then determined by solving the Lorentz equation, whilst the photon follows a ballistic trajectory. EPOCH enables pair-production via the Breit-Wheeler and trident processes. The simulations presented in this study are run without the trident process, given that the cross-section for this process, both in the laser field and the Coulomb field of a hydrogenic nucleus, is negligibly small.

2.2. Simulation parameters

A series of 2D PIC simulations were run in order to scan over various geometric configurations of the counter-propagating laser pulses. The simulation grid had dimensions 200 μm $\times$ 28.8 μm, initialised with 9984×1440 cells in the x and y directions, respectively. The target was a 100 μm-thick slab of proton plasma (extended in the y-

direction to the dimensions of the simulation grid) with a density of $n_e = 10n_c$, where $n_c = \frac{m_e \epsilon_0 \omega_L^2}{e^2}$ is the critical density, with ϵ_0 the vacuum permittivity and ω_L the laser frequency. The driving laser for the interaction was a circularly polarised pulse with a peak intensity $I_L = 1 \times 10^{23}$ Wcm^{-2} (i.e., $a_0 = \sqrt{2}a_z = \sqrt{2}a_y = \frac{eE_L}{m_e c \omega_L} \simeq 282$), wavelength $\lambda_L = 1$ μm, and focused to a spot size of 5 μm FWHM. The pulse also had a Gaussian temporal profile with a full width half max (FWHM) duration of 10 fs (in order to be consistent with the pulse duration possible at APOLLON [1]). The γ-ray beam then interacts with counter-propagating laser pulses in various configurations, which will be described in a later section. These laser pulses enter the grid at an angle equal to the divergence half-angle of the γ-ray beam, as measured at the point of interaction from an initial simulation with no counter-propagating pulses. The laser pulses were initialised with Gaussian temporal and spatial profiles, with FWHM values of 30 fs and 3 μm, respectively, and a peak intensity of 4×10^{23} Wcm^{-2} for each pulse. An external magnetic field was applied across the target, in the direction of laser propagation (for the driving laser), with a dimensionless magnitude $\left(\hat{B_x} \equiv \frac{eB_x}{m_e \omega_L}\right) = 0.1a_0$. Preliminary simulations demonstrated that the application of such a magnetic field guides the energetic electrons accelerating through the target, and therefore reduces the divergence half-angle of the emitted radiation relative to the case with no external field. A similar effect, by which photon emission is enhanced via self-generated magnetic fields during laser-solid interactions, has been reported in Refs. [32, 33] and described theoretically in Refs. [34, 35]. The peak magnitude of the external magnetic field corresponds to a field strength of 10^8 G. It has been demonstrated in Ref. [36] that a longitudinal magnetic field of this magnitude may be generated via the inverse Faraday effect, driven by RR. Ref. [36] employs similar laser and target parameters to this study (the laser intensity varies in the range $I_L = (1.9 - 16.7) \times 10^{23}$ Wcm^{-2} and the target is hydrogenic plasma with density $90n_c$), demonstrating the feasibility of generating such strong magnetic fields in numerical simulations of laser-solid interactions. However, we must additionally note that the method of magnetic field generation described in Ref. [36] is not directly applicable to the pair-production scheme described in this article, given that the driving laser induces density gradients within the plasma and therefore violates the requirement of a homogeneous plasma in describing the generation of the γ-ray beam.

The point at which the laser pulses interact with the γ-ray beam was chosen to be 10 μm behind the target rear surface, such that the entire temporal profile of the counter-propagating pulses can interact with the γ-ray beam before striking the target rear. The cases in which the laser pulses propagate at an angle were compared to a conventional case, in which a single laser with a peak intensity 8×10^{23} Wcm^{-2} (and the same pulse duration and focal spot size) interacts with the γ-ray beam head-on.

3. Results

3.1. Stage 1 - Properties of the γ-ray beam

3.1.1. Formation of the γ-ray beam. During the interaction of an ultra-intense laser pulse with a solid target, the laser ponderomotive force pushes electrons into the target skin depth, ℓ_s, the distance over which the laser field decays to $1/e$ of its peak magnitude. The skin depth is written $\ell_s = c\sqrt{\gamma_e}/\omega_{p,e}$, where $\omega_{p,e} = \sqrt{n_e e^2/\epsilon_0 m_e}$ is the plasma frequency, n_e is the electron number density and γ_e is the electron Lorentz factor. The laser-solid interaction then produces an overdense electron bunch in front of the laser pulse, and a region of depleted electron density behind it. As the electrons are driven forwards, a charge imbalance builds up, establishing an electric field across the depletion zone, which acts to accelerate the ions. This forms a double layered structure, driven forwards by laser radiation pressure, known as the laser-piston [37, 38]. Due to the high laser intensities involved in this study, the electrons escaping from the charge depletion zone lose a significant fraction of their energy through radiation emission, and therefore experience strong RR. This is associated with a reduction in the piston velocity ($c\beta_p$) and less efficient acceleration of the reflected ions [39, 40, 41, 42]. In the semi-classical regime, this reduction in the efficiency of the process of radiation pressure acceleration (RPA) may be interpreted as a decrease of the reflection coefficient, $\mathcal{R} = \frac{1-\beta_p}{1+\beta_p} - \frac{(1-\cos\langle\theta_\gamma\rangle)\langle\mathcal{E}_\gamma\rangle}{2(1-\beta_p)} \leq \frac{1-\beta_p}{1+\beta_p}$ [40]. An expression for the recession velocity of the plasma surface, $c\beta_p$, under the influence of RR is derived in Ref. [40] such that $\beta_p = \frac{\Omega}{\Omega+1}\mathcal{F}(\langle\mathcal{E}_\gamma\rangle, \Omega, \langle\theta_\gamma\rangle)$ where $\Omega = \sqrt{\frac{n_c}{n_i}\frac{m_e}{Zm_e+m_i}}\frac{a_0}{\sqrt{2}}$ and $\mathcal{F}(\langle\mathcal{E}_\gamma\rangle, \Omega, \langle\theta_\gamma\rangle)$ is a decreasing function over Ω and $\langle\mathcal{E}_\gamma\rangle$ (See an explicit form for $\mathcal{F}_{\langle\theta\rangle\simeq 90^\circ}$ in Ref. [40]). The term $\langle\mathcal{E}_\gamma\rangle$ is the fraction of laser energy converted into synchrotron radiation, and Ω is a dimensionless parameter which depends on the target ion charge-to-mass ratio and density. Here, $\langle\theta_\gamma\rangle$ is the average absolute value of the radiation emission angle over all space.

It has been demonstrated in Ref. [43] that the angular distribution of the emitted radiation in this regime is strongly dependent on the target ion mass. For a deuterium plasma, for example, the increased ion mass leads to an enhancement in the amplitude of the charge separation field, since it takes longer for the heavy ions to respond to the charge imbalance within the plasma [43, 44]. In the case of a proton plasma target, the amount of radiation is reduced and it is predominantly produced in the forwards direction. This radiation is emitted primarily along the direction of laser propagation, compared to other hydrogenic targets such as deuterium and tritium plasmas. We therefore choose a dense proton plasma slab as the target for this study, as this reduces the magnitude of the RR effects on the piston velocity. Due to the high target velocities which can be achieved in this regime, the forward emitted radiation is Doppler boosted, by the factor $\mathcal{D}$ [45];

$$\mathcal{D} \equiv \mathcal{D}\left(\langle\beta\rangle, \theta\right) = \frac{\sqrt{1-\langle\beta\rangle^2}}{1-\langle\beta\rangle\cos\theta} \tag{1}$$

where θ is the polar angle defined relative to the laser propagation axis, and $\langle\beta\rangle$ is the average velocity of electrons within the target, which in the hole boring regime of RPA (i.e. for targets with thickness much greater than the skin depth) may be approximated as $\langle\beta\rangle \simeq \beta_p$. For the target and laser parameters used in this study, radiation emitted at the average absolute emission angle is Doppler shifted by a factor $\mathcal{D} \simeq 2$. It is found that the relativistic Doppler effect boosts the average energy of the forwards directed photons in the simulations presented in this paper, such that the photons within the γ-ray beam have an average energy $\sim$10 MeV.

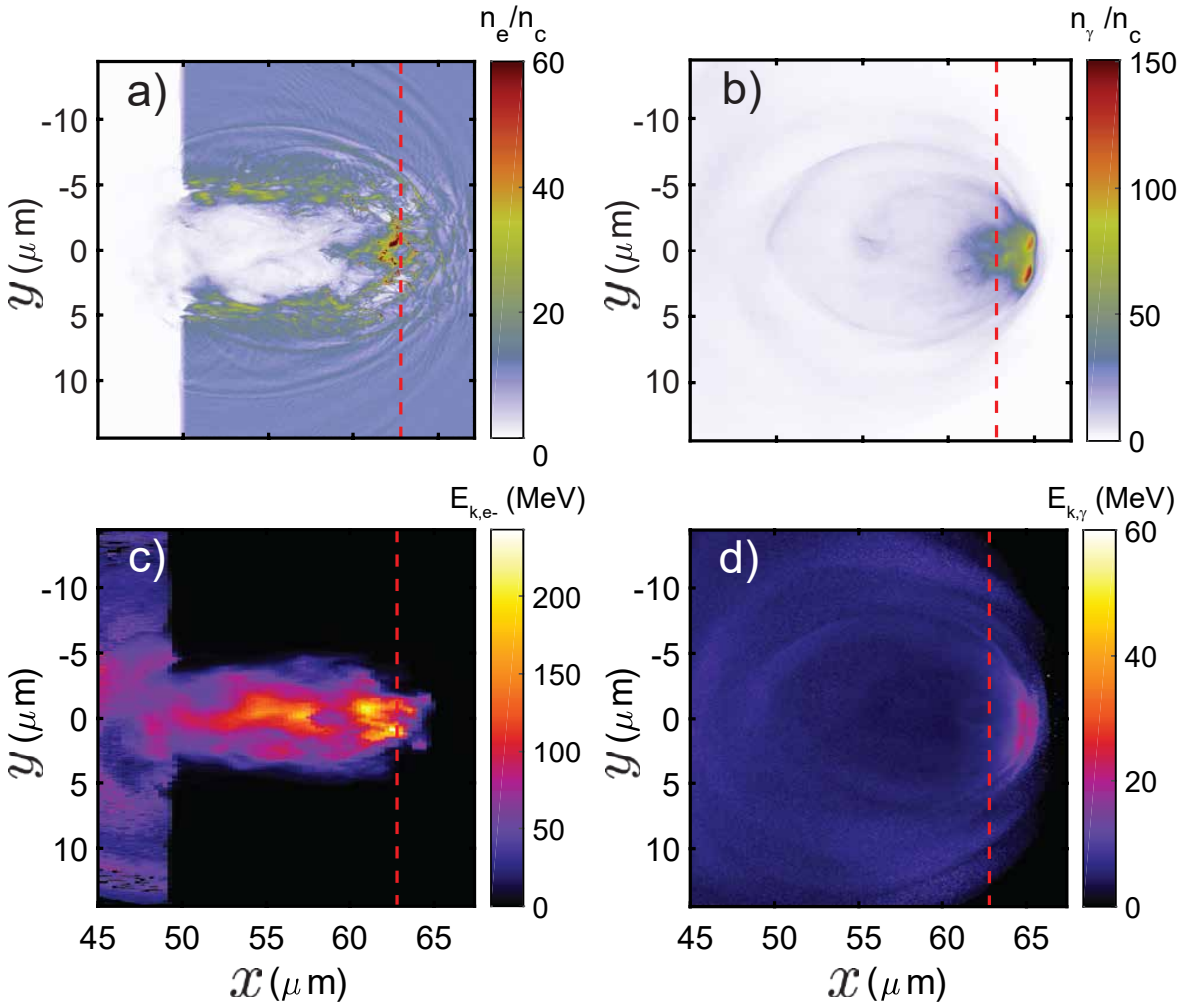

Figure 1. Simulation results illustrating the formation of the γ-ray beam. (a)-(b) Spatial distribution of the electron and photon number densities, normalised to the critical density. (c)-(d) Spatial distribution of the electron and photon kinetic energies, in units of MeV. The red dashed line indicates the position of the peak of the laser E_y field. All plots are taken at a time of 15 laser periods ($t = 15T_L$).

Fig. 1 (a), shows the spatial distribution of the electron density, demonstrating the overdense electron surface being driven through the target in the hole boring regime of RPA. The dashed red line represents the position of the peak of the laser E_y field (i.e. the position where the magnitude of the absolute value of E_y is maximised). Panel (b)

shows a similar plot for the photon number density, in which it is clear that the high energy photons originate from the charge depletion zone, in which the laser field decays in magnitude (i.e. in front of the peak represented by the dashed red line). Panels (c) and (d) further demonstrate this principle, showing the spatial distributions of the electron and photon kinetic energies, respectively. The divergence half-angle of the γ-ray beam is calculated from the angular distribution of the photons which are located within 2 μm of the target rear, at the time at which the peak photon density crosses the target rear surface. The divergence half-angle of the γ-ray beam is found to be $\sim 10^{\circ}$ (as demonstrated in Fig. 6).

Stage 2 - Investigating counter-propagating laser configurations for pair-production

The forward emitted photons within the γ-ray beam then interact with counter-propagating laser pulses, as shown in Fig. 2. We propose that a more efficient configuration (in terms of total number and energy of the produced positrons) can be achieved by using two pulses propagating at an angle with respect to the photons emerging from the target. This is due to the fact that, whilst the photons emerge from the target rear as a high energy γ-ray beam, this beam is slowly diverging. During the head-on interaction with a counter-propagating, focusing laser pulse, there is a relatively small number of photons in the laser focal spot, and therefore a low probability for pair-production. Instead, we propose using two counter-propagating pulses with the same total energy as for the head-on interaction. The two pulses propagate along the divergence half-angle of the γ-ray beam, such that there is a larger spatial overlap compared to a head-on interaction. The divergence half-angle, $\langle\theta_j\rangle/2$, is defined in terms of an average emission angle, $\langle\theta_j\rangle$, as follows:

$$\theta_j = \arctan\left(\frac{p_{y,j}}{p_{x,j}}\right) \tag{2}$$

$$\langle\theta_j\rangle = \frac{2}{N}\Sigma_{k=1}^{N}|\theta_{j,k}| \tag{3}$$

where $p_{y,j}$ and $p_{x,j}$ are the transverse and longitudinal momenta for species $j \in \{\gamma, pos\}$, where γ denotes photons and *pos* denotes positrons. The second equation then describes the average of the absolute value of the emission angle over N macroparticles within the system. Note that it is necessary to consider the absolute value, since the distributions are typically symmetric.

We investigate four different interaction geometries in order to determine the properties of the emitted positrons. These configurations are shown schematically in Fig. 2, and are described as follows; configuration (i) uses two 4×10^{23} Wcm^{-2} linearly polarised pulses, (ii) uses two 4×10^{23} Wcm^{-2} circularly polarised pulses, with the electric field vectors rotating in the same direction, (iii) again uses two 4×10^{23} Wcm^{-2} circularly polarised pulses but in this case the electric fields rotate in opposite directions, and (iv) uses one head-on interaction with a circularly polarised pulse of intensity 8×10^{23} Wcm^{-2}. The laser pulses have a FWHM duration of 30 fs, and each one is focused to a

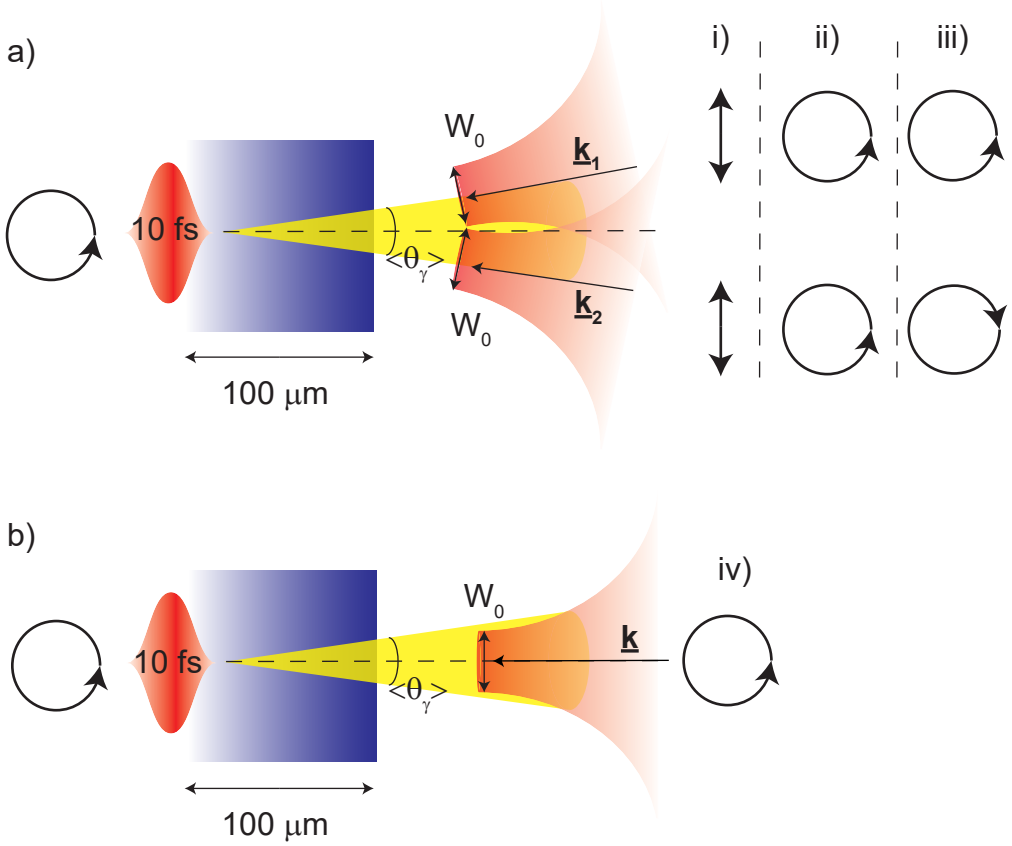

Figure 2. A schematic of the different interaction configurations. All cases use a circularly polarised, 10 fs FWHM pulse, with a peak intensity of 1×10^{23} Wcm^{-2}, to generate the γ-ray beam. (a) The γ-ray beam then interacts with two lasers, propagating along the divergence half-angle of the emitted radiation. (i)-(iii) Three different polarisation configurations for the counter-propagating lasers are investigated. (b) These cases are compared to a single pulse, with the same energy, interacting head-on with the γ-ray beam.

focal spot of 3 μm FWHM diameter, in order to match the area covered by the slowly diverging γ-ray beam at the point of interaction. It is important to note that this final case has the same total energy as the other configurations, but it would be expected that the quantum parameters, χ_e and χ_γ, are maximised due to the head-on interaction geometry. The quantum parameters are defined such that:

$$\chi_e = \frac{\gamma_e}{E_{crit}} |\mathbf{E}_\perp + \boldsymbol{\beta}_e \times c\mathbf{B}|, \tag{4}$$

$$\chi_\gamma = \frac{\hbar\omega}{2m_e c^2 E_{crit}} |\mathbf{E}_\perp + \hat{\mathbf{k}} \times c\mathbf{B}|, \tag{5}$$

where γ_e is the electron Lorentz factor, $\mathbf{E}_\perp$ is the component of the electric field perpendicular to the electron velocity, $\boldsymbol{\beta}_e$ is the electron velocity normalised to the speed of light, $\hat{\mathbf{k}}$ is the photon unit wavevector and $\hbar\omega$ is the photon energy.

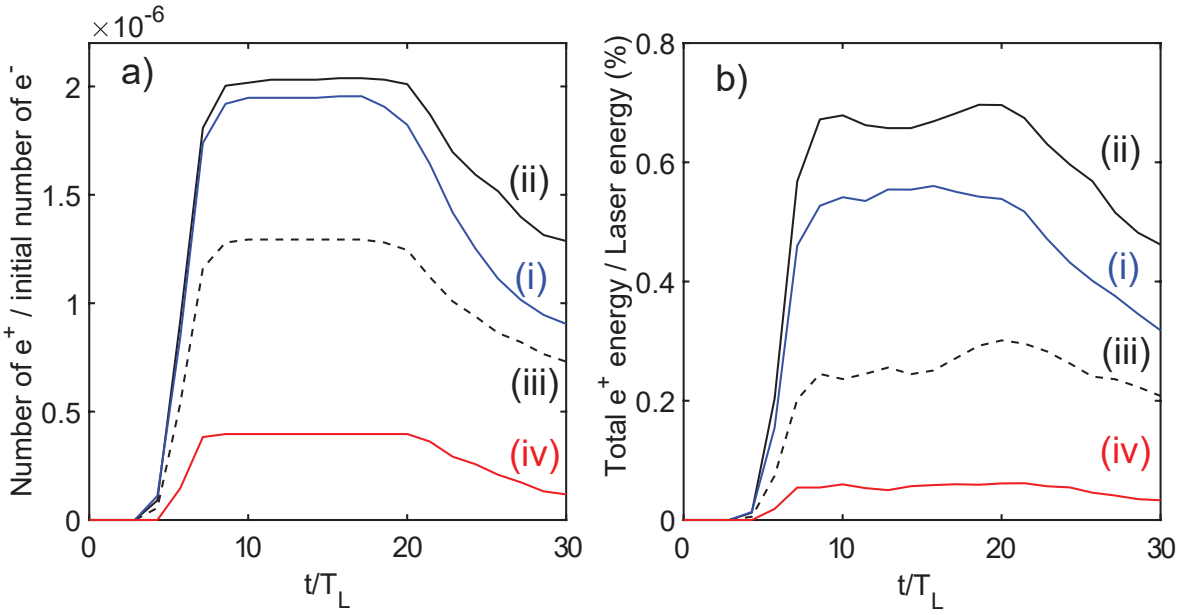

Figure 3. (a) Number of positrons normalised to the initial number of electrons in the system, as a function of time. Time is stated in units of laser periods, with $t = 0$ indicating the time at which the γ-ray beam emerges from the target rear. Each colour represents a different configuration of the counter-propagating laser pulses. (b) Total positron energy normalised to the laser energy, as a function of time.

3.1.2. The influence of the laser field configuration on the produced positrons. The number and total energy of the positrons produced for each of the four described configurations is shown in Fig. 3. The top panel shows the number of positrons normalised to the initial number of electrons in the system, as a function of time. The time is expressed in units of the laser period, with $t = 0$ corresponding to the time at which the γ-ray beam escapes from the target rear. Positrons are first produced as the γ-ray beam interacts with the rising edge of the laser pulses. These come into focus at the interaction point at $\sim 10T_L$, leading to a plateau in the number of positrons. At later times, the number of positrons decreases, as they are accelerated by the laser fields and leave the system. These positrons also emit copious amounts of synchrotron-like photons, leading to a decrease in the positron energy with time. Fig. 3 (a) shows that the largest number of positrons is produced for configuration (ii), two circularly polarised pulses with the electric fields rotating in the same direction. It is interesting to observe that there is a significant reduction in the number of positrons produced compared to the optimal configuration, when the electric fields rotate in the opposite direction (comparing configurations (iii) and (ii)). A similar effect has been described in Ref. [46] in the head-on collision of two circularly polarised pulses. The number of positrons produced using linearly polarised laser pulses (configuration (i)) is only marginally lower than that of the best case configuration.

Despite the fact that the total energy content for the single pulse head-on interaction (configuration (iv)) is the same as the two-pulse configurations, the number of positrons

is reduced by approximately a factor of four relative to the best case. This is a counter-intuitive result, since we would expect that this is the interaction geometry which maximises the electron and photon quantum parameters. The difference between these cases will be explained in terms of an analytical estimate, which describes the electric field configurations at the point of interaction, later in this article. Fig. 3(b) shows the total positron energy as a function of time, normalised to the total energy contained within the driving pulse and the two counter-propagating pulses. We note that the energy of the produced positrons is also maximised for the case of two circularly polarised pulses with the same rotation direction. This gives close to an order of magnitude increase in the total positron energy compared to the head-on interaction (configuration (iv)) with the same total laser energy.

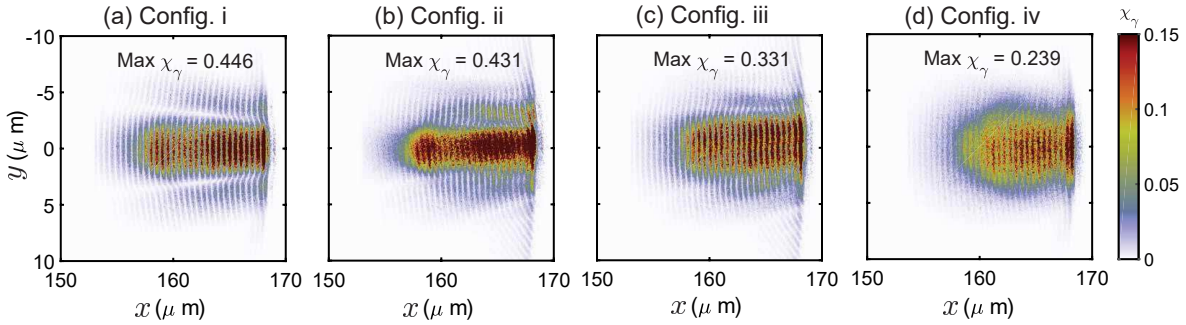

Figure 4. (a)-(d) Spatial distribution of the photon quantum parameter, χ_γ, for the four interaction geometries, all compared at the time at which the number of positrons in the system is maximised. The four configurations are as follows; (a) two 4×10^{23} Wcm^{-2} linearly polarised pulses, (b) two 4×10^{23} Wcm^{-2} circularly polarised pulses with the same rotation directions, (c) two 4×10^{23} Wcm^{-2} circularly polarised pulses with opposite rotation directions, and (d) one 8×10^{23} Wcm^{-2} circularly polarised pulse, interacting head-on with the γ-ray beam. The maximum χ_γ value for each case is displayed at the top of the panel.

Whilst configuration (ii) produces the highest number of positrons, we note that the dual pulse interaction geometry may be difficult to implement experimentally. It is then reasonable to investigate whether there are other single pulse configurations which could be employed to improve the yield of positrons. In addition to configurations (i)-(iv), we also investigated a configuration in which the focal spot size (of a single, circularly polarised laser pulse) was doubled, to a FWHM diameter of 6 μm. To maintain the same total pulse energy as in the previous simulations, the intensity of the pulse was decreased to 4×10^{23} Wcm^{-2}. The reasoning behind this configuration is that the increased laser spot size may enable a large degree of spatial overlap between the γ-ray beam and the counter-propagating laser pulse, but this comes at the cost of lower laser intensity. We found in this case that the total positron yield was decreased to $\sim 10\%$ of configuration (ii), whilst the total positron energy was reduced to 3%. We also investigated a configuration in which a single pulse, with the same total energy and

focal spot size as configuration (iv), collided with the γ-ray beam at an angle (equal to the divergence half-angle of the γ-ray beam). The purpose of this configuration is to investigate if the two pulse interaction geometry is not experimentally feasible, whether it is better to use a single pulse in a head-on interaction or to interact with the γ-ray beam at an angle. We found that this geometry produced $\sim 10\%$ more positrons than configuration (iv), however it performed poorly in comparison to configurations (i)-(iii), producing only $\sim 19\%$ of the number of positrons of configuration (ii). The dual pulse interaction geometry therefore produces a higher yield of positrons than any of the single pulse configurations under investigation.

Referring back to configurations (i)-(iv), there are numerous factors which may account for the differences in positron yield, such as the structure of the laser fields and the amount of spatial and temporal overlap between the laser pulses and the γ-ray beam. The dual pulse interaction configurations are designed such that the overlap between the laser pulses and the γ-ray beam is higher than for the head-on interaction, that is, $\frac{\langle\theta_\gamma\rangle}{2} = |\theta_1| = |\theta_2|$ (where θ_1, θ_2 are the incidence angles of the counter-propagating pulses) as shown in Fig. 5. This higher degree of overlap can account for the differences between configuration (iv) and the two pulse configurations.

Differences in the electric field structure at the interaction point can also be investigated through the spatial distribution of the photon quantum parameter. Fig. 4 panels (a)-(d) show the photon quantum parameter, χ_γ, as a function of space, for each of the four configurations, (i) to (iv) respectively. In each case the rear of the target is located at 150 μm, so we can be confident that the positrons are produced at the interaction point, and not from the laser pulses striking the target rear.

The differences between the various configurations are striking in Fig. 4. Configuration (ii), which produced the highest number of positrons, is seen to produce a spatially localised structure in the distribution of χ_γ. There are both a high number of counts and high χ_γ values observed within this feature, therefore accounting for the enhanced number of positrons produced in this case. We briefly comment on the fact that this case also gave rise to strong radiative trapping of electrons at the interaction point. This radiative trapping has been described in detail in Refs. [47, 48]. Its context within the dual pulse interaction scheme is beyond the scope of this study. For now, we state that the enhancement in the number of trapped electrons leads to the production of electron-positron pairs through the decay of hard photons, emitted from the electrons, interacting with the counter-propagating laser pulses. The linear polarisation case gives rise to a higher maximum χ_γ value, however the spatially localised structure in the χ_γ distribution is not as prominent. Finally, we see in panel (d) that the head-on interaction, which produced the lowest number of positrons, also gives the lowest χ_γ values. The spatial overlap between the laser pulse and the γ-ray beam is lower for this configuration compared to the others, leading to less trapping of the electrons and a reduced number of positrons. The degree of electron trapping, and hence the formation of a spatially localised feature in the distribution of χ_γ, is enhanced for the dual pulse interaction geometry with circularly polarised pulses, compared to a head-on interaction.

We therefore propose that this configuration could be applied to boost the probability of pair cascades at higher laser intensities. Provided that quantum stochastic effects can be neglected during the interaction, it may also be possible to use this configuration to trigger pair cascades by colliding ultra-intense laser pulses with electron beams generated via LWFA.

3.1.3. Determining the positron production mechanism. There are multiple pair-production mechanisms which can occur in multi-PW laser-plasma interactions, which are described in more detail in the appendix. We stress that the electron-positron pairs produced in this study are generated via the non-linear Breit-Wheeler (NLBW) process. The Bethe-Heitler and trident processes are negligible in comparison to the NLBW process, due to the choice of a low-Z target (where Z is the atomic number of the plasma). The cross section for the trident process within the laser field [49, 50] is negligible in comparison to the trident process in the field of a high-Z nucleus, and in any case the simulations were run with this process turned off.

To distinguish between the pairs produced via the interaction of the counter-propagating laser pulses and the γ-ray photons, and those produced in the interaction of the laser pulses with the escaping electrons, we performed the simulations presented in the previous section, this time using a modified version of EPOCH in which the electrons are prevented from radiating after a user defined cut-off time. After this time, the optical depths for photon emission from the electrons and positrons are no longer updated. This time corresponds to when the peak photon density crosses the target rear. In these simulations, even if the electrons reach the interaction point, they cannot radiate photons. Any positrons produced in this configuration must therefore arise due to the interaction of the γ-ray beam with the laser pulses.

The results of this investigation are summarised in table 1. For each of the four configurations (see Fig. 2), the percentage of the number of positrons produced via the interaction of photons within the γ-ray beam and the counter-propagating laser pulses, is calculated. The total number of positrons comes from the simulations using the unmodified version of EPOCH, i.e. the results presented in Fig. 3. A similar quantity is presented for the total energy of the positrons produced. To be clear, in this section we are distinguishing the positrons produced via the the interaction of the γ-ray beam with the laser pulses, from those produced by the interaction of the laser pulses with hard photons, radiated by escaping electrons.

The key result from table 1 is that the configuration which previously produced the highest total number of positrons (configuration (ii); two 4×10^{23} Wcm^{-2} circularly polarised pulses, with the same rotation direction), now produces the lowest number of positrons via interaction with the γ-ray photons. Given that this configuration also produced the highest number of trapped electrons, this suggests that the majority of positrons come from the decay of hard photons emitted by the trapped electrons. The configuration which previously produced the lowest total number of positrons, now produces the highest number of positrons via interaction with the γ-ray beam. Since

this configuration produced the fewest trapped electrons, we deduce that a lower number of trapped electrons leads to less positron production, however more of the positrons will come from the interaction of the counter-propagating laser pulses with the γ-ray beam. The same trend occurs in terms of the positron energy; for configuration (iv), over 50% of the total positron energy is produced via interaction with the γ-ray beam, whereas this drops to only 14% for configuration (ii).

This result could be verified experimentally, by utilising a combination of collimators and strong magnets at the target rear in order to deflect the escaping electrons, ensuring that only photons from the γ-ray beam give rise to pair-production during interaction with the counter-propagating laser pulses.

Configuration	**(i)**	**(ii)**	**(iii)**	**(iv)**
Number of e^+ produced via interaction with the γ-ray beam (%)	79	45	60	84
Energy of e^+ produced via interaction with the γ-ray beam (%)	40	14	17	56

Table 1. A table showing the percentage of positrons produced from the interaction of the counter-propagating laser pulses with photons in the γ-ray beam, compared to the total number of positrons produced, for each of the four configurations.

3.1.4. Features of the different configurations. In the previous section, we have shown that due to the divergence of the γ-ray beam, the number of positrons produced within the dual beam interaction scheme is enhanced when the laser pulses propagate at an angle. This angle is chosen to match the divergence half-angle of the γ-ray beam, in order to maximise the spatial overlap. We will reproduce this result using an analytical estimate, by demonstrating that the dual pulse geometry produces a higher average χ_γ compared to a head-on interaction with a single laser pulse.

We consider two counter-propagating laser pulses, which propagate with angles θ_1 and θ_2 with respect to the x-direction. These angles are equal to the divergence half-angle of the γ-ray beam, measured just before the point of interaction. These two pulses have the same total energy and spot size as the laser pulses used in the simulations. A schematic of this interaction geometry is provided in Fig. 5.

The propagation of these two pulses (denoted by α=1,2) are described by the wave vectors $\hat{\mathbf{k}}_\alpha = (-\cos\theta_\alpha, \mp\sin\theta_\alpha, 0)$. The polarised electromagnetic fields associated with these pulses are then given in Eqs. 6 and 7, below.

$$\frac{e\mathbf{E}_\alpha}{m_e c\omega_L} = a_\alpha \left(\cos\phi_\alpha \hat{\mathbf{y}}_\alpha + \delta_\alpha \sin\phi_\alpha \hat{\mathbf{z}}\right), \tag{6}$$

$$\frac{e\mathbf{B}_\alpha}{m_e \omega_L} = a_\alpha \left(-\delta_\alpha \sin\phi_\alpha \hat{\mathbf{y}}_\alpha + \cos\phi_\alpha \hat{\mathbf{z}}\right) \tag{7}$$

In the above expressions, $a_\alpha \simeq 380\Theta$, where $\Theta = \sqrt{2}$ for linear polarisation and $\Theta = 1$ for circular polarisation. In addition, $-1 \leq \delta_\alpha \leq 1$ (where $\delta_\alpha = 0$ corresponds to linear

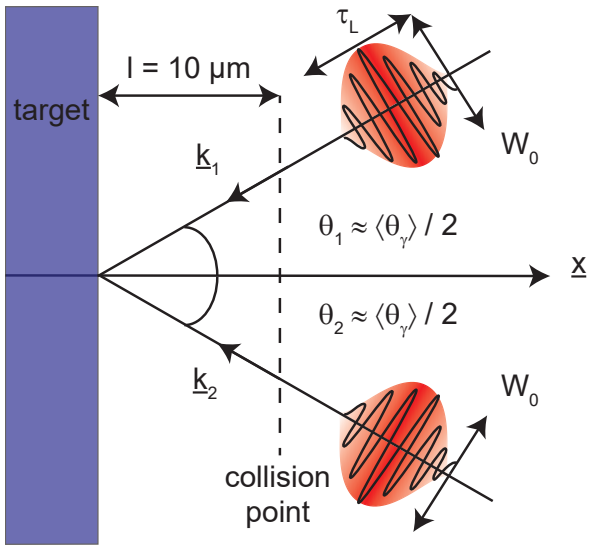

Figure 5. Schematic showing the geometry used to model the dual pulse interaction. Two laser pulses interact with the γ-ray beam, propagating at angles $|\theta_1| = |\theta_2| = |\langle\theta_\gamma\rangle|/2 \approx 10^\circ$ with respect to the x-direction.

polarisation and ± 1 corresponds to the right and left handed circular polarisations, respectively) and $\phi_\alpha = \omega_L t - \mathbf{k}_\alpha \cdot \hat{\boldsymbol{r}}$ is the phase for each laser pulse, such that $\hat{\boldsymbol{r}} = \hat{\mathbf{x}} + \hat{\mathbf{y}} + \hat{\mathbf{z}}$ and $\mathbf{k}_\alpha . \hat{\mathbf{y}}_\alpha = \mathbf{k}_\alpha . \hat{\mathbf{z}} = 0$. Using these expressions, the photon quantum parameter may be expressed as:

$$\chi_\gamma \approx \gamma_\gamma a_\alpha \mathcal{G}\mathcal{H}\frac{\hbar\omega_L}{m_e c^2} \tag{8}$$

where, $\gamma_\gamma \equiv \frac{\hbar\omega_\gamma}{m_e c^2} \sim \frac{\hbar\omega_{cr}}{m_e c^2}$ is the photon equivalent Lorentz factor, estimated from the photon spectrum critical frequency, $\omega_{cr} = \frac{3}{2}\frac{\gamma_e^3 \|\mathbf{p}_e \times \mathbf{F}_L\|}{\mathbf{p}_e^2}$ such that $\gamma_\gamma \sim \frac{\hbar\omega_{cr}}{m_e c^2} \sim \gamma_e^2 a_0 \frac{\hbar\omega_L}{m_e c^2} \approx 20$. The functions $\mathcal{G}$ and $\mathcal{H}$ are defined as follows. The function $\mathcal{H}$ accounts for the finite size of the laser spot and may be written as:

$$\mathcal{H} \equiv \exp\left[-\frac{l^2}{w_0^2}\left(\tan\theta - \tan\frac{\langle\theta_\gamma\rangle}{2}\right)^2\right] \tag{9}$$

where l is the distance from the rear of the target to the interaction point and FWHM$= 2\sqrt{\ln 2} w_0 \simeq 3$ μm is the spot size. If the distance from the target rear to the interaction point is short then the γ-ray beam will not diverge significantly, and so a pulse propagating head-on with the beam will interact with a significant number of photons. When designing experiments however, it is ideal to have the interaction point further back from the target rear, so that the properties of the photons and produced positrons can be probed by external diagnostics. In this case, the divergence of the γ-ray beam, coupled with the finite spot size of the laser, will significantly reduce the average χ_γ value.

The function $\mathcal{G}$ which appears in Eq. (8) is defined from $\mathcal{G}^2 \equiv \sum_{\alpha=1}^{2} a_\alpha^{-2}\left[\mathbf{F}_{L,\alpha}^2 - \left(\frac{\hbar\mathbf{k}_\gamma}{m_e c}.e\mathbf{E}_\alpha\right)^2\right]$, where $\mathbf{F}_{L,\alpha}$ is the Lorentz force associated with the

fields of each laser pulse. In order to obtain a quantity comparable to the simulation results, it is necessary to average $\mathcal{G}^2$ over the course of a laser period. The average of a quantity, $\mathcal{A}$, over the phase of each of the pulses, is given by $\bar{\mathcal{A}} \equiv \frac{1}{(2\pi)^2}\int_0^{2\pi}\int_0^{2\pi}\mathcal{A}d\phi_1 d\phi_2$. Performing this average for the quantity $\mathcal{G}^2$ yields:

$$\begin{aligned}\bar{\mathcal{G}}^2 &= 2 + \Delta + 2\beta_x\cos\theta(1+\delta) \\ &+ \beta_x^2(\Delta\cos^2\theta - \sin^2\theta) + \beta_y^2(\Delta\sin^2\theta - \cos^2\theta)\end{aligned} \tag{10}$$

where, $\delta \equiv \frac{1}{2}(\delta_1 + \delta_2)$, $\Delta \equiv \frac{1}{2}(\delta_1^2 + \delta_2^2)$, and β_x and β_y are projections of the photon velocity, such that $\beta_x = \cos\frac{\langle\theta\rangle}{2}$ and $\beta_y = \sin\frac{\langle\theta\rangle}{2}$.

Evaluating the above expression for the dual pulse interaction ($|\theta| = |\theta_1| = |\theta_2| = \frac{|\langle\theta_\gamma\rangle|}{2}$) and a head-on, single pulse interaction ($\theta = 0$), yields:

$$\begin{aligned}\bar{\mathcal{G}}^2(\theta = \langle\theta_\gamma\rangle/2) &= 2 + \Delta + 2(1+\delta)\cos^2\frac{\langle\theta_\gamma\rangle}{2} \\ &+\Delta\Big(\cos^4\frac{\langle\theta_\gamma\rangle}{2} + \sin^4\frac{\langle\theta_\gamma\rangle}{2}\Big) - \frac{1}{2}\sin^2\langle\theta_\gamma\rangle\end{aligned} \tag{11}$$

$$\bar{\mathcal{G}}^2(\theta = 0) = 2(1+\Delta) + 2(1+\delta)\cos\frac{\langle\theta_\gamma\rangle}{2} - (\Delta+1)\sin^2\frac{\langle\theta_\gamma\rangle}{2}. \tag{12}$$

For a circularly polarised pulse interacting head-on with the γ-ray beam (Eq. (12)), we must account for the spot size effect, and find that this case predicts the lowest χ_γ value. Using the above estimates of $\bar{\mathcal{G}}^2$, it is possible to evaluate Eq. (8), such that averaging over a laser period for each of the four configurations produces the following results:

$$\sqrt{\bar{\chi_\gamma^2}} = \begin{cases} 0.0425 & : \text{config. (i)} \\ 0.0426 & : \text{config. (ii)} \\ 0.0366 & : \text{config. (iii)} \\ 0.0299 & : \text{config. (iv)} \end{cases}$$

The above values demonstrate that the analytical estimates follow the same trend as the simulation results. First, we see a significant reduction in $\sqrt{\bar{\chi_\gamma^2}}$ for the head-on interaction geometry, compared to the dual pulse configurations. It is also clear that we have demonstrated the difference between the two circular polarisation cases, since $\sqrt{\bar{\chi_\gamma^2}}$ is lower for the case where the two laser pulses have opposite rotation directions. We also show that the linear polarisation case produces a slightly lower $\sqrt{\bar{\chi_\gamma^2}}$ value compared to the best circularly polarised case. This estimate is in agreement with Refs. [51, 52], in which it is demonstrated that the radiated power from an electron oscillating in a linearly polarised pulse (in vacuum) is reduced compared to the case for circular polarisation. This is due to the fact that χ_e and χ_γ depend on the projection of the momentum along the direction of the wavevector of the background field, which is minimised in the case of linear polarisation due to acceleration of electrons along the polarisation direction.

4. Discussion

In this final section, we compare our results with more conventional configurations, which are likely to be among the first experiments conducted at multi-PW laser facilities [54]. In this paper we have explored the dual pulse interaction geometry, and have concluded that the interaction of a high energy γ-ray beam (with an average photon energy ~ 10 MeV) with two circularly polarised pulses, with their electric fields rotating in the same direction, produces the largest total number of positrons (i.e. configuration (ii)). Whilst this configuration produced the highest overall number of positrons, we have demonstrated that most of these positrons come from the interaction of the counter-propagating laser pulses with high energy photons radiated by the trapped electrons. As benchmark simulations (against which the conventional configurations are compared), we therefore use configuration (ii), with the modified and un-modified versions of EPOCH. These are referred to as benchmarks 1 and 2, respectively, for the remainder of this section. We remind the reader that in the modified code, the electrons which escape the rear of the target are unable to radiate, and therefore the positrons which are produced in this case come from the interaction of the counter-propagating laser pulses with the γ-ray beam.

The benchmark simulations are compared with two configurations in which there is no initial step of generating the γ-ray beam, instead the ultra-intense laser pulse impacts the solid target directly. The specific configurations used are; (v) the interaction of one ultra-intense pulse, with the same total energy content as the driving laser plus the counter-propagating laser pulses in configuration (ii) (analogously to Ref. [53]), and (vi) the interaction of two laser pulses, each with half the total energy of configuration (v), directly onto the target. The target used in both of these cases is the same 100 μm-thick proton plasma slab described in the previous sections. The conventional configurations described here are easier to implement experimentally, however as we will describe, lead to a less optimised positron source.

In terms of the total number and energy of the produced positrons, configuration (v) performed the best, producing approximately five times more positrons than benchmark 1, and an order of magnitude more positrons than benchmark 2. In terms of the total positron energy, configuration (v) produced approximately five times higher energy compared to benchmark 1. The dual pulse interaction performed more favourably when compared to configuration (vi) (i.e. two counter-propagating pulses, incident on either side of the target). Here, we found that benchmark 1 produced three times more positrons, with six times higher total energy, compared to configuration (vi). In addition, benchmark 2 yielded approximately the same number of positrons as configuration (vi). It is important to note that a significant fraction of these positrons come from the interaction of the colliding pulses with photons radiated by the trapped electrons. The comparison of the conventional cases with benchmark 1 is the most relevant result, as future laser-solid experiments are unlikely to be able to easily separate the positrons produced via the aforementioned mechanisms.

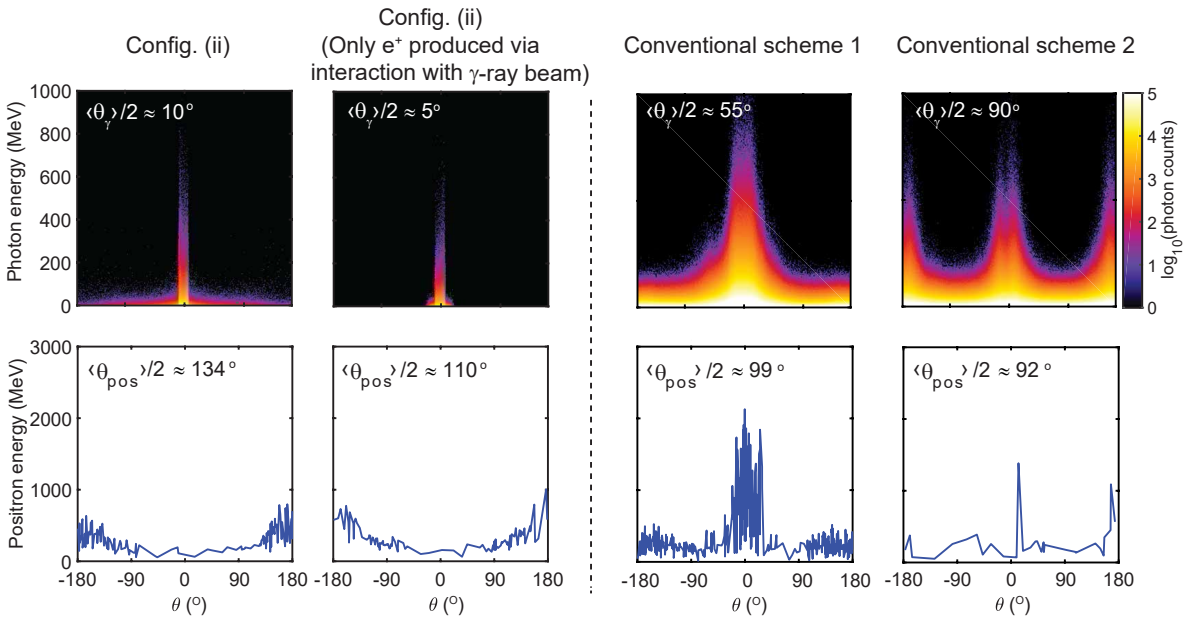

Figure 6. Plots comparing the dual pulse interaction geometry with two conventional schemes, i.e. configurations (v) and (vi). Conventional scheme 1 is the interaction of a 8.5×10^{23} Wcm^{-2} pulse directly with a target, whilst conventional scheme 2 is the interaction of two 4.25×10^{23} Wcm^{-2} pulses with a target in a directly counter-propagating geometry. The top panels show the photon angular distributions, with the average absolute emission angle value displayed in the top left corner, whilst the lower panels show the positron angular distributions. All plots are calculated at the time when the number of positrons in the system is maximised.

The results described above lead to important experimental prospectives. The most prolific numbers of positrons, in this study, were produced via the direct interaction of an ultra-intense pulse (8.5×10^{23} Wcm^{-2}) with a thick target. Obtaining the energy in a single pulse is beyond the normal capability of multi-PW laser facilities under development (i.e. in the absence of additional measures to enhance the intensity further, such as the use of ellipsoidal plasma mirrors [55, 56]). Experiments in the near future are therefore more likely to use a setup comparable to configuration (vi), in which two lower intensity pulses interact in a directly counter-propagating geometry with a solid target. We propose that the dual pulse interaction is more efficient than configuration (vi), producing a larger number of positrons with a higher total energy (although a significant fraction of these are produced via the interaction of the laser pulses with electrons trapped at the interaction point).

It is important, however, to emphasize the fact that the proposed dual pulse interaction geometry is also beyond the capability of current experiments. This is due to the fact that the γ-ray beam generated in this article is collimated via the application of an external magnetic field of magnitude 10^8 G. Such a strong magnetic field has not been generated experimentally to date. However, it has been shown numerically in Ref. [36] that a field of the required orientation and magnitude can be generated

via ultra-intense laser-solid interactions. In addition, before the dual pulse interaction geometry can be employed experimentally, it is necessary to determine how sensitive it is to fluctuations in the laser parameters. These may include spatial jitter, temporal lag, and misalignments in the focusing, all of which will impact the overlap between the γ-ray beam and the counter-propagating laser pulses. The effect of the laser temporal intensity contrast on the positron yield is another aspect which should be considered before this scheme can be employed experimentally. This parameter is negligible with respect to the driving beam; given that this interacts with a 100 μm-thick plasma slab, the target should remain opaque to the laser pulse throughout the interaction, therefore enabling the γ-ray beam sufficient time to form. In addition, increasing the target thickness will mitigate the effects of the whole target expansion driven by insufficient temporal intensity contrast. Finally, we note that the low target density required for this scheme ($10n_c$) can currently be realised in the form of foams or aerogels. However, these targets typically have inhomogeneous density profiles. We propose that a more uniform density profile could be produced by first irradiating the foam target with X-rays. In addition, these foams often contain high-Z elements, such as carbon and silicon, however it is feasible that low density hydrogen foams could be developed.

The emitted photon and positron angular distributions are also important features to compare between the conventional configurations and the dual pulse interaction geometry. The photon angular distribution gives an indication of the direction in which the positrons are most likely to be emitted. This is useful in terms of experimental measurements, since the number of positron counts will be significantly lower than those of the photons and therefore more difficult to detect. The aim is to generate a low divergence positron source which could, for example, be used for laboratory astrophysics experiments.

Fig. 6 compares the benchmark cases with two conventional schemes (configurations (v) and (vi)), in terms of the photon and positron angular distributions (top and bottom rows, respectively). All of these distributions are compared at the time in the interaction at which the number of positrons is maximised. Firstly, looking at the photon angular distributions, we see that the γ-ray beam generated in the dual pulse interaction geometry remains highly collimated. For benchmark 1, the divergence half-angle is $\langle\theta_\gamma\rangle/2 \sim 10^\circ$, whilst for benchmark 2, this angle decreases to $\sim 5^\circ$. The photon angular distribution for configuration (v) has a much larger divergence half-angle, whilst for configuration (vi) the distribution is almost isotropic, with $\langle\theta_\gamma\rangle/2 \sim 90^\circ$. For these conventional cases, the emission comes primarily from electrons ejected from the laser focal spot, driving a substantial amount of the radiation along the direction parallel to the target surface.

Comparing the positron angular distributions, again we see that the conventional schemes give rise to approximately isotropic distributions, which closely follow those of the photons. An isotropic distribution is not particularly useful experimentally, since it is generally not possible to measure the number of positron counts over all of the 4π emission, and sampling over a small solid angle may result in a significant reduction

in the number of counts. Secondly, it is impractical to use an isotropic distribution for collisions with counter-propagating laser pulses or relativistic particle sources, since the flux of positrons within the sampled solid angle is low. The dual pulse interaction geometry produces positrons at large angles, with a large degree of anisotropy. This is particularly evident in benchmark 1, in which case the positron divergence half-angle is $\langle\theta\rangle_{pos}/2$=134°. This distribution is favourable for experiments, since the positron source can be collided with counter-propagating lasers, and may be easier to detect given that the positrons are emitted close to the laser axis.

Next generation laser facilities, such as ELI-NP, will utilise two 10 PW laser pulses [54], in which case the interaction geometry is likely to be similar to configuration (vi). The results presented in this article predict that higher positron numbers and energies can be obtained using the dual pulse interaction geometry, if such a set up is possible experimentally (i.e. if the proposed magnetic field magnitude can be obtained via laser-solid interactions, and the robustness of the scheme to fluctuating laser parameters can be determined). A further advantage our scheme offers is that the emitted positron distribution is significantly more anisotropic than any of the conventional configurations which were explored, therefore providing a useful experimental tool. When even higher intensity lasers are possible (at intensities of the order 10^{24} Wcm^{-2}), prolific numbers of positrons will be produced through the direct interaction of the pulse with a solid target, albeit producing a more isotropic positron source compared to the dual pulse interaction.

Finally, we briefly discuss the limitations of the QED-PIC approach taken in this study. EPOCH does not account for spin polarisation effects, discussed in references [57, 58], which may influence the cross sections for the pair production mechanisms. We also performed the simulations without accounting for the trident process; whilst this is negligible for the target parameters in this study, this will not be the case for higher ion mass targets which will likely be employed experimentally. We also comment on the fact that the QED-PIC simulations apply the constant cross fields approximation, which assumes that the laser fields can be treated as a static background [59, 60]. Whilst this is typically a valid assumption for ultra-intense laser pulses, where $a_0 \gg 1$, this may not hold in the case where the pulses have a varying temporal profile. Since the constant cross fields approximation is used in the pair-production rates, this is a consideration which should be accounted for when comparing the results of this article to those obtained experimentally.

5. Conclusions

We have investigated non-linear Breit-Wheeler pair-production using a dual pulse interaction geometry, which employs intensities which will be realised at multi-PW laser facilities. The first stage in the proposed scheme is the generation of a γ-ray beam via an ultra-intense laser-solid interaction. The divergence half-angle of the γ-ray beam is reduced via the application of an external magnetic field (such that

the divergence half-angle $\sim 10^{\circ}$) and the average photon energy is enhanced via the relativistic Doppler effect to $\sim$ 10 MeV. In the second stage of the interaction, the γ-ray beam interacts with counter-propagating laser pulses, inducing non-linear pair-production. The laser parameters which produced the highest number of positrons and the highest total positron energy, were two circularly polarised laser pulses, with the electric fields rotating in the same direction.

Whilst the dual pulse interaction geometry, utilising two circularly polarised pulses (with the same rotation direction), produced the highest total number of positrons it was found that these are produced predominantly via radiative trapping of electrons and positrons at the point of interaction. This proposed scheme will, however, enable the study of the NLBW process at upcoming multi-PW laser facilities.

Finally, we demonstrated that our dual pulse interaction geometry performs better than a configuration in which two directly counter-propagating pulses collide directly with a thick target, in terms of the total number and energy of the positrons produced. This is an important consideration, since experiments at next generation facilities will likely try such a geometry. Our proposed interaction geometry has the distinct advantage that the positrons are produced in an anisotropic distribution, compared to the isotropic emissions from direct laser interactions with solid targets. Such positron sources could be used for laboratory astrophysics experiments.

Acknowledgments

This work was funded by the UK EPSRC (grant numbers EP/M018091/1, EP/R006202/1, EP/P007082/1 and EP/M018156/1). We also acknowledge the use of the EPOCH PIC code (developed under EPSRC grant EP/G054940/1) and both the Archie-WeST (www.archie-west.ac.uk) and ARCHER supercomputers, with access to ARCHER provided via the Plasma Physics HEC Consortia grant: (EP/R029148/1). Data associated with research published in this paper is accessible at: https://doi.org/10.15129/bf892dcb-9566-4cb6-b700-7bdad09a32d0.

Appendix

A1. Underpinning theory

The acceleration of electrons in ultra-intense laser fields leads to the emission of synchrotron-like radiation, causing an electromagnetic back reaction force to act on the electrons. The classical description of this so-called radiation reaction (RR) as a frictional force is valid provided that the magnitude of the RR force, evaluated in the electron rest frame, is much less than that of the Lorentz force [61, 4]. In this case the equation of motion is the Landau-Lifshitz (LL) equation which is expressed, to first order in γ_e^2, as follows:

$$\frac{d}{dt}\mathbf{p}_e = \mathbf{F}_{L,e} - \frac{P_\gamma}{c}\boldsymbol{\beta}_e \tag{13}$$

where $\mathbf{p}_e$ is the electron momentum, $\boldsymbol{\beta}_e$ is the electron velocity normalised to the speed of light, $\gamma_e = (1 - \beta_e^2)^{-1/2}$ is the electron Lorentz factor and $\mathbf{F}_{L,e} = -e(\mathbf{E} + c\boldsymbol{\beta}_e \times \mathbf{B})$ is the Lorentz force. The magnitude of the RR force (the second term on the right) is related to photon emission through the electron radiated power, P_γ:

$$P_\gamma = \frac{2\alpha c}{3\lambda\!\!\!^{-}_c} g\left(\chi_e\right) \chi_e^2 m_e c^2 \tag{14}$$

Here, α is the fine structure constant, and $\lambda\!\!\!^{-}_c$ is the reduced Compton wavelength. The radiated power from a single electron is expressed in terms of a Lorentz invariant quantity, χ_e, which describes the importance of quantum effects, and is defined as follows:

$$\chi_e = \frac{\gamma_e}{E_{crit}} |\mathbf{E}_\perp + \boldsymbol{\beta}_e \times c\mathbf{B}| \tag{15}$$

where $\mathbf{E}_\perp$ is the component of the electric field perpendicular to the electron velocity and E_{crit} is the Sauter-Schwinger critical field.

As discussed, the classical framework describes the electron trajectory when the magnitude of the RR force is much less than that of the Lorentz force, as evaluated in the electron rest frame. When the magnitude of these two forces are comparable in the laboratory frame, the electron loses a significant fraction of its kinetic energy through radiation emission, over the course of a laser period. This case is known as the classical radiation dominated regime, in which the emission is treated as a continuous process consisting of a large number of photons [62, 63, 64, 65, 66].

The quantum radiation dominated regime arises when the radiation is emitted in the form of a few high energy photons. The classical view of RR as a smooth frictional force acting at every point along the electron trajectory no longer holds. Instead, we require a stochastic description which accounts for the fact that the electron has a probability at each point on its trajectory of emitting a high energy photon, and that the trajectory will become discontinuous as a result of this emission process.

When photon emission is re-interpreted as a stochastic effect, the magnitude of the RR force is reduced compared to the classical description provided in Eq. (13). In the stochastic emission model, a photon cannot be emitted with energy greater than the electron kinetic energy. This imposes a hard cut off in the tail of the photon energy spectrum, relative to the classical case of continuous radiation emission, and therefore reduces the electron radiated power. Since it is the high energy photons which contribute most to the RR force, we see a subsequent reduction in the magnitude of this force. To account for this, the electron radiated power (Eq. (14)) is reduced by a stochastic scaling factor, $g(\chi_e) = (3.7\chi_e^3 + 31\chi_e^2 + 12\chi_e + 1)^{-4/9}$, as defined in Refs. [67, 68]. From the expression for $g(\chi_e)$, we can see that for a value of $\chi_e = 0.1$, the stochastic scaling factor reduces the electron radiated power by a factor of 2/3. This approach of scaling the electron radiated power approximates the quantum nature of photon emission, but does not include other important quantum effects such as pair-production; the regime of $\chi_e \simeq 0.1$ is therefore referred to as semi-classical.

As $\chi_e \to 1$, the magnitude of the electric field in the electron rest frame tends towards the critical field strength, and quantum effects dominate the interaction. In this regime, the electrons radiate hard photons, which have a high probability of generating electron-positron pairs. To evaluate the probability of pair-production in an intense laser field it is necessary to introduce a second Lorentz invariant parameter, the photon quantum parameter:

$$\chi_\gamma = \frac{\hbar\omega}{2m_e c^2 E_{crit}} |\mathbf{E}_\perp + \hat{\boldsymbol{k}} \times c\mathbf{B}|. \tag{16}$$

In the above equation, $\mathbf{E}_\perp$ is the electric field in the direction perpendicular to the unit wave vector, $\hat{\boldsymbol{k}}$, which describes the direction of photon propagation. The parameter χ_γ characterises the probability of pair-production when a photon with wavevector $\hat{\boldsymbol{k}}$ interacts with a stationary, uniform field as described in Ref. [30].

A2. Synchrotron-like radiation

The acceleration of electrons to ultra-relativistic energies results in the production of synchrotron-like radiation, which is emitted into a narrow cone along the direction of the electron momentum. The spectral intensity of the radiation emitted by a single electron, per unit solid angle, is defined as follows:

$$\frac{d^2 I_\gamma}{d\Omega d\omega} = \frac{P_\gamma}{\omega_{cr}} \delta(\boldsymbol{\Omega} - \mathbf{p}_e/||\mathbf{p}_e||) \mathcal{F}(\chi_e, \chi_\gamma) \tag{17}$$

The delta function in Eq. (17) describes the beam-like nature of the emission. The term ω_{cr} is the critical frequency for the synchrotron emission, which is related to the rotation frequency of the radiating electron in the laser fields, given by $\omega_r = |\mathbf{p}_e \times \mathbf{F}_{L,e}|/p_e^2$, such that $\omega_{cr} = \frac{3}{2}\omega_r \gamma_e^2$. The function $\mathcal{F}(\chi_e, \chi_\gamma)$ is the quantum emissivity [69, 30]. In the case where $\chi_\gamma \ll \chi_e < 1$, this reduces to the MacDonald function, $\mathcal{F}(\omega/\omega_{cr}) = \frac{9\sqrt{3}}{8\pi} \frac{\omega}{\omega_{cr}} \int_{\omega/\omega_{cr}}^{\infty} K_{5/3}(x) dx$, where $K_{5/3}$ is a modified Bessel function.

A3. Pair-production mechanisms

Pair-production at multi-PW laser facilities is likely to be dominated by two mechanisms; the decay of high energy photons of synchrotron-like radiation, or by the non-linear Breit-Wheeler process described in the equation below.

$$\gamma + n\gamma_L \to e^+ + e^- \tag{18}$$

Here, γ represents a probe photon, in our case a photon in the high energy γ-ray beam, whilst γ_L denotes a photon of the laser. The non-linear Breit-Wheeler process therefore describes the interaction of a probe photon with n photons from the laser. This is the dominant process in ultra-intense laser-plasma interactions, where the non-linearity arises due to both the high flux of photons within the laser focal spot, and the high energy of the photons within the γ-ray beam. The non-linear Breit-Wheeler process has

been observed during the collision of an ultra-relativistic electron beam with a counter-propagating laser pulse, for example, in the SLAC E144 experiment. The two stage, dual pulse interaction geometry presented in this article offers a means to investigate the non-linear Breit-Wheeler process through laser-solid interactions.

We briefly mention that there is also a linear Breit-Wheeler process, which describes pair-production via the interaction of two high energy photons. Whilst this process is fundamental to extreme astrophysical phenomena, the cross section for this mechanism occurring during ultra-intense laser-plasma interactions is negligibly small, due in part to the fact that the linear Breit-Wheeler process requires the collision of high energy photons at a large angle of incidence (i.e. a head-on collision) [70, 32, 30].

There are however additional pair-production processes which can be relevant in laser-plasma interactions; these are the Bethe-Heitler and trident processes [71, 72]. The Bethe-Heitler process has been used to generate pair plasmas in several reported studies. In this process, a high energy photon (for example, within the γ-ray beam) decays in the Coulomb field around a high-Z nucleus. The decay process is more likely to occur here than in vacuum, since there are more ways in which the photon can partition its energy, for example, by interaction with the nucleus. The number of pairs produced by this process can be suppressed through the choice of a low-Z target, such as cryogenic hydrogen. There is also the trident process, in which an electron scatters off an external (laser) field, producing a photon. This photon then interacts with the (laser) field, subsequently producing electron-positron pairs [49, 50]. If the external field is the Coulomb field of the target nuclei, then the contribution from the trident process is reduced through the choice of a hydrogenic target. In our case, the external field is that of the laser. The trident process is negligible here due to the low photon energies associated with the laser field.

References

[1] J. P. Zou, C. Le Blanc, D. Papadopoulos, G. Chériaux, P. Georges, G. Mennerat, F. Druon, L. Lecherbourg, A. Pellegrina and P. Ramirez, High Power Laser Science and Engineering **3**, E2, (2015)
[2] D. Habs, T. Tajima, and V. Zamfir, Nuclear Physics News **21**, 23-29, (2011)
[3] P. A. Dirac, Proc. R. Soc. A **167**, 148-69, (1938)
[4] L. D. Landau and E. M. Lifshitz, The Classical Theory of Fields 4th Edition (New York, Pergamon), (1994)
[5] L. Ji, A. Pukhov, E. N. Nerush, I. Y. Kostyukov, B. F. Shen, and K. U. Akli, Phys. Plasmas **21**, 023109, (2014)
[6] M. Tamburini, F. Pegoraro, A. Di Piazza, C. H. Keitel and A. Macchi, New J. Phys. **12**, 123005, (2010)
[7] M. J. Duff, R. Capdessus, D. Del Sorbo, C. P. Ridgers, M. King and P. McKenna, Plasma Phys. Control. Fusion **60**, 064006, (2018)
[8] A. Di Piazza, Phys. Rev. Lett. **117**, 213201, (2016)
[9] K. Krajewska and J. Z. Kamiński, Phys. Rev. A. **86**, 052104, (2012)
[10] G. Breit and J. A. Wheeler, Phys. Rev. **46**, 1087, (1934)

[11] F. Sauter, Z. Phys. **69**, 742, (1931)
[12] J. Schwinger, Phys. Rev. **82**, 664, (1951)
[13] B. B. Pollock, C. E. Clayton, J. E. Ralph, F. Albert, A. Davidson, L. Divol, C. Filip, S. H. Glenzer, K. Herpoldt, W. Lu and K. A. Marsh, Phys. Rev. Lett. **107**, 045001, (2011)
[14] T. G. Blackburn, C. P. Ridgers, J. G. Kirk and A. R. Bell, Phys. Rev. Lett. **112**, 015001, (2014)
[15] G. M. Samarin, M. Zepf, and G. Sarri, J. Mod. Opt. **65**, 1362, (2018)
[16] T. N. Wistisen, A. DiPiazza, H. V. Knudsen and U. I. Uggerhøj, Nat. Comm. **9**, 795, (2018)
[17] J. M. Cole, K. T. Behm, E. Gerstmayr, T. G. Blackburn, J. C. Wood, C. D. Baird, M. J. Duff, C. Harvey, A. Ilderton, A. S. Joglekar, K. Krushelnick, S. Kuschel, M. Marklund, P. McKenna, C. D. Murphy, K. Poder, C. P. Ridgers, G. M. Samarin, G. Sarri, D. R. Symes, A. G. R. Thomas, J. Warwick, M. Zepf, Z. Najmudin and S. P. D. Mangles, Phys. Rev. X **8**, 011020, (2018)
[18] K. Poder, M. Tamburini, G. Sarri, A. DiPiazza, S. Kuschel, C. D. Baird, K. Behm, S. Bohlen, J. M. Cole, D. J. Corvan, M. J. Duff, E. Gerstmayr, C. H. Keitel, K. Krushelnick, S. P. D. Mangles, P. McKenna, C. D. Murphy, Z. Najmudin, C. P. Ridgers, G. M. Samarin, D. R. Symes, A. G. R. Thomas, J. Warwick and M. Zepf, Phys. Rev. X **8**, 031004, (2018)
[19] G. Sarri, K. Poder, J. M. Cole, W. Schumaker, A. DiPiazza, B. Reville, T. Dzelzainis, D. Doria, L. A. Gizzi, G. Grittani, S. Kar, C. H. Keitel, K. Krushelnick, S. Kuschel, S. P. D. Mangles, Z. Najmudin, N. Shukla, L. O. Silva, D. R. Symes, A. G. R. Thomas, M. Vargas, J. Vieira and M. Zepf, Nat. Comm. **6**, 6747, (2015)
[20] H. Chen, F. Fiuza, A. Link, A. Hazi, M. Hill, D. Hoarty, S. James, S. Kerr, D. D. Meyerhofer, J. Myatt, J. Park, Y. Sentoku and G. J. Williams, Phys. Rev. Lett. **114**, 215001, (2015)
[21] D. L. Burke, R. C. Field, G. Horton-Smith, J. E. Spencer, D. Walz, S. C. Berridge, W. M. Bugg, K. Shmakov, A. W. Weidemann, C. Bula, and K. T. McDonald, Phys. Rev. Lett. **79**, 1626, (1997)
[22] C. Bamber, S. J. Boege, T. Koffas, T. Kotseroglou, A. C. Melissinos, D. D. Meyerhofer, D. A. Reis, W. Ragg, C. Bula K. T. McDonald, E. J. Prebys, D. L. Burke, R. C. Field, G. Horton-Smith, J. E. Spencer, D. Walz, S. C. Berridge, W. M. Bugg, K. Shmakov and A. W. Weidemann, Phys. Rev. D **60**, 092004, (1999)
[23] A. Hartin, A. Ringwald and N. Tapia, Phys. Rev. D **99**, 036008, (2019)
[24] B. King and N. Elkina, Phys. Rev. A **94**, 062102, (2016)
[25] A. Ilderton and M. Marklund, J. Plasma Phys. **82**, 655820201, (2016)
[26] O. J. Pike, F. Mackenroth, E. G. Hill, and S. J. Rose, Nat. Photonics **8**, 434, (2014)
[27] H. Z. Li, T. P. Yu, J. J. Liu, Y. Yin, X. L. Zhu, R. Capdessus, F. Pegoraro, Z. M. Sheng, P. McKenna, and F. Q. Shao, Sci. Rep. **7**, 17312, (2017)
[28] J. Q. Yu, H. Y. Lu, T. Takahashi, R. H. Hu, Z. Gong, W. J. Ma, Y. S. Huang, C. E. Chen and X. Q. Yan, Phys. Rev. Lett. **122**, 014802, (2019)
[29] T. D. Arber, K. Bennett, C. S. Brady, A. Lawrence-Douglas, M. G. Ramsay, N. J. Sircombe, P. Gillies, R. G. Evans, H. Schmitz, A. R. Bell and C. P. Ridgers, Plasma Phys. Control. Fusion **57**, 113001, (2015)
[30] J. G. Kirk, A. R. Bell, and I. Arka, Plasma Phys. Control. Fusion **51**, 085008, (2009)
[31] V. Baier and V. Katkov, Sov. Phys. JETP **26**, 854, (1968)
[32] O. Jansen, T. Wang, D. J. Stark, E. d'Humieres, T. Toncian and A. V. Arefiev, Plasma Phys. and Control. Fusion **60**, 054006, (2018)
[33] D. J. Stark, T. Toncian and A. V. Arefiev, Phys. Rev. Lett. **116**, 185003, (2016)
[34] Z. Gong, F. Mackenroth, T. Wang, X. Q. Yan, T. Toncian and A. V. Arefiev, arXiv:1811.00425, (2018)
[35] Z. Gong, F. Mackenroth, X. Q. Yan and A. V. Arefiev, arXiv:1905.02152, (2019)
[36] T. V. Liseykina, S. V. Popruzhenko and A. Macchi, New J. Phys. **18**, 072001, (2016)
[37] T. Schlegel, N. Naumova, V. T. Tikhonchuk, C. Labaune, I. V. Sokolov and G. Mourou, Phys. Plasmas **16**, 083103, (2009)
[38] A. P. L. Robinson, P. Gibbon, M. Zepf, S. Kar, R. G. Evans and C. Bellei, Plasma Phys. Control.

Fusion **51**, 024004, (2009)
[39] J. G. Kirk, A. R. Bell, and C. P. Ridgers, Plasma Phys. Control. Fusion **55**, 095016, (2013)
[40] R. Capdessus and P. McKenna, Phys. Rev. E **91**, 053105, (2015)
[41] E. N. Nerush and I. Y. Kostyukov, Plasma Phys. Control. Fusion **57**, 035007, (2015)
[42] D. Del Sorbo, D. R. Blackman, R. Capdessus, K. Small, C. Slade-Lowther, W. Luo, M. J. Duff, A. P. L. Robinson, P. McKenna, Z. M. Sheng and J. Pasley, New J. Phys. **20**, 033014, (2018)
[43] R. Capdessus, E. d'Humières and V. T. Tikhonchuk, Phys. Rev. Lett. **110**, 215003, (2013)
[44] R. Capdessus, M. Lobet, E. d'Humieres and V. T. Tikhonchuk, Phys. Plasmas, **21**, 123120, (2014)
[45] R. Capdessus, M. King, D. Del Sorbo, M. J. Duff, C. P. Ridgers and P. McKenna, Sci. Rep. **8**, 9155, (2018)
[46] T. Grismayer, M. Vranic, J. L. Martins, R. A. Fonseca, and L. O. Silva, Phys. Plasmas **23**, 056706, (2016)
[47] A. Gonoskov, A. Bashinov, I. Gonoskov, C. Harvey, A. Ilderton, A. Kim, M. Marklund, G. Mourou and A. Sergeev, Phys. Rev. Lett. **113**, 014801, (2014)
[48] A. Gonoskov, A. Bashinov, S. Bastrakov, E. Efimenko, A. Ilderton, A. Kim, M. Marklund, I. Meyerov, A. Muraviev and A. Sergeev, Phys. Rev. X **7**, 041003, (2017)
[49] V. Dinu and G. Torgrimsson, Phys. Rev. D **97**, 036021, (2018)
[50] F. Mackenroth and A. DiPiazza, Phys. Rev. D **98**, 116002, (2018)
[51] S. S. Bulanov, T. Z. Esirkepov, A. G. R. Thomas, J. Koga and S. V. Bulanov, Phys. Rev. Lett. **105**, 220407, (2010)
[52] V. F. Bashmakov, E. N. Nerush, I. Y. Kostyukov, A. M. Fedotov and N. B. Narozhny, Phys. Plasmas **21**, 013105, (2014)
[53] C. P. Ridgers, C. S. Brady, R. Duclous, J. G. Kirk, K. Bennett, T. D. Arber, A. P. L. Robinson and A. R. Bell, Phys. Rev. Lett. **108**, 165006, (2012)
[54] I. C. E. Turcu, C. Murphy, F. Negoita, D. Stutman, M. Zepf, J. Schreiber, C. Harvey, R. J. Gray, M. Toma, S. Balascuta and G. Sarri, Rom. Rep. Phys. **68**, S145, (2016)
[55] M. Nakatsutsumi, A. Kon, S. Buffechoux, P. Audebert, J. Fuchs and R. Kodama, Opt. Lett. **35**, 2314, (2010)
[56] R. Wilson, M. King, R. J. Gray, D. C. Carroll, R. J. Dance, C. Armstrong, S. J. Hawkes, R. J. Clarke, D. J. Robertson, D. Neely and P. McKenna, Phys. Plasmas **23**, 033106, (2016)
[57] B. King, N. Elkina and H. Ruhl, Phys. Rev. A **87**, 042117, (2013)
[58] B. King, Phys. Rev. A **91**, 033415, (2015)
[59] A. Ilderton, B. King and D. Seipt, arXiv preprint arXiv:1808.10339, (2018)
[60] A. Di Piazza, M. Tamburini, S. Meuren and C. H. Keitel, Phys. Rev. A **99**, 022125, (2019)
[61] J. D. Jackson, Classical Electrodynamics (New York, Wiley), 464, (1999)
[62] J. Koga, T. Z. Esirkepov and S. V. Bulanov, Phys. Plasmas **12**, 093106, (2005)
[63] A. Di Piazza, K. Z. Hatsagortsyan, and C. H. Keitel, Phys. Rev. Lett. **102**, 254802, (2009)
[64] S. V. Bulanov, T. Z. Esirkepov, J. Koga and T. Tajima, Plasma Phys. Reports **30**, 196, (2004)
[65] I. V. Sokolov, N. M. Naumova and J. A. Nees, Phys. Plasmas **18**, 093109, (2011)
[66] N. Neitz and A. Di Piazza, Phys. Rev. Lett. **111**, 054802, (2013)
[67] C. P. Ridgers, J. G. Kirk, R. Duclous, T. G. Blackburn, C. S. Brady, K. Bennett, T. D. Arber and A. R. Bell, Journal Comp. Phys. **260**, 273, (2014)
[68] C. P. Ridgers, T. G. Blackburn, D. Del Sorbo, L. E. Bradley, C. Slade-Lowther, C. D. Baird, S. P. D. Mangles, P. McKenna, M. Marklund, C. D. Murphy and A. G. R. Thomas, J. Plasma Phys. **83**, 715830502, (2017)
[69] T. Erber, Rev. Mod. Phys. **38**, 626, (1966)
[70] X. Ribeyre, E. d'Humières, O. Jansen, S. Jequier, V. T. Tikhonchuk, and M. Lobet, Phys. Rev. E **93**, 013201, (2016)
[71] H. Hu, C. Müller and C. H. Keitel, Phys. Rev. Lett. **105**, 080401, (2010)
[72] A. Ilderton, Phys. Rev. Lett. **106**, 020404, (2011)